Microglia constitute a barrier that prevents neurotoxic protofibrillar Aβ42 hotspots around plaques

Carlo Condello[1,3,*], **Peng Yuan**[1,2,*], **Aaron Schain**[1,4], and **Jaime Grutzendler**[1,2,#]

[1]Department of Neurology, Yale University, New Haven, CT 06511, USA

[2]Department of Neurobiology, Yale University, New Haven, CT 06510, USA

Abstract

In Alzheimer's disease (AD), β-amyloid (Aβ) plaques are tightly enveloped by microglia processes, but the significance of this phenomenon is unknown. Here we show that microglia constitute a barrier with profound impact on plaque composition and toxicity. Using high-resolution confocal and *in vivo* two-photon imaging in AD mouse models, we demonstrate that this barrier prevents outward plaque expansion and leads to compact plaque microregions with low Aβ42 affinity. Areas uncovered by microglia are less compact but have high Aβ42 affinity, leading to formation of protofibrillar Aβ42 hotspots that are associated with more severe axonal dystrophy. In aging, microglia coverage is reduced, leading to enlarged protofibrillar Aβ42 hotspots and more severe neuritic dystrophy. *CX3CR1* gene deletion or anti-Aβ immunotherapy causes expansion of microglia coverage and reduced neuritic dystrophy. Failure of the microglia barrier and the accumulation of neurotoxic protofibrillar Aβ hotspots may constitute novel therapeutic and clinical imaging targets for AD.

INTRODUCTION

The mechanisms by which neural circuit disruption occurs in Alzheimer's disease (AD) are not well understood. While genetic evidence in early onset familial AD suggests a strong involvement of abnormal β-amyloid (Aβ) processing and aggregation[1], in sporadic late onset AD it is thought that disturbed Aβ clearance may lead to Aβ aggregation[2], neuronal injury and dysfunction[3]. A variety of mechanisms of brain Aβ clearance have been postulated[4–6] including a role for microglia[7], the resident immune and phagocytic cell in the central nervous system. The involvement of these cells in AD is further supported by recent studies

[#]Corresponding author: Jaime Grutzendler (jaime.grutzendler@yale.edu).
[3]Current address: Institute for Neurodegenerative Diseases, University of California, San Francisco, USA
[4]Current address: Beth Israel Deaconess Medical Center, Harvard Medical School, Boston, MA, USA
[*]Authors contributed equally

showing that human genetic variants in microglia-related molecules, such as *TREM2* and *CD33* are associated with increased risk of late onset AD[8–12].

Microglia are highly motile cells that constantly survey the brain microenvironment and undergo activation in response to a diverse range of tissue perturbations[13,14]. One striking feature of the behavior of microglia in the AD brain is their marked clustering around fibrillar Aβ deposits, which are also in close proximity to dendrites with reduced spine density and dystrophic axons[15–19]. Plaque-associated microglia display an activated and polarized morphology with their processes pointed towards and highly intertwined with the plaque surface[16,20,21]. Despite this close interaction, *in vivo* mouse data has shown that microglia are very ineffective at phagocytosis of fibrillar amyloid deposits[16,19,22] but are instead able to take up pre-fibrillar forms of Aβ[7,19]. Additionally, modulation of microglia-related chemokine receptors or anti-Aβ immunization, both of which can affect microglia activation status, have been shown to influence the degree of brain amyloid accumulation[18,19,23–30]. While these effects on amyloid burden may partly be explained by Aβ phagocytosis[19], microglia could possess additional unknown functions that may affect the evolution of amyloid deposition. Furthermore, due to their close proximity to axonal structures and their potential for producing neurotoxic cytokines and reactive oxygen species[31], some suggest that microglia play a causative role in the formation of dystrophic neurites. On the other hand, microglia could play neuroprotective roles through mechanisms not yet identified[32]. Thus, it remains unknown whether aspects of microglia function play beneficial or detrimental roles that could be specifically targeted for therapeutic purposes.

To address this gap in knowledge, we developed *in vivo* methods using two-photon and high-resolution confocal microscopy for examining the role of microglia in the dynamic equilibrium between soluble interstitial Aβ and fibrillar amyloid deposits, amyloid plaque expansion and the resulting toxicity to adjacent neurons. Our data reveal a striking pattern of anti-colocalization between microglia processes, protofibrillar Aβ42 and dystrophic axons. We demonstrate that this pattern is due to microglia acting as a barrier that restricts the radial expansion of plaques by controlling their affinity for soluble Aβ, a function that we show is critical for limiting the formation of neurotoxic hotspots of protofibrillar Aβ42 around plaques. Modulation of microglia activity by either *CX3CR1* receptor deletion or passive anti-Aβ immunization leads to expansion of the microglia barrier with a consequent reduction in plaque neurotoxicity. Finally, we show that certain natural and synthetic small molecules have the ability to selectively target these neurotoxic protofibrillar Aβ42 hotspots, raising the possibility that analogous compounds could be used therapeutically or in clinical imaging applications.

RESULTS

Microglia plaque envelopment does not prevent diffusion of soluble Aβ into the plaque core

We first quantified the extent to which the surface of individual amyloid plaques was covered by the processes of adjacent microglia in two Alzheimer-like transgenic mouse models (5xFAD and CRND8). In our analysis of confocal image stacks of brain slices with labeled microglia and fibrillar amyloid plaques, we observed that larger plaques tended to

have less microglia coverage than smaller ones, but overall there was a great heterogeneity in the degree of microglia coverage (Fig. 1 a–b). Given that microglial processes are known to be highly motile in the normal brain[13], we next asked how physically stable the processes involved in tightly wrapping plaques were compared to those that did not contact plaques. To address this, we used *in vivo* two-photon imaging to visualize plaques and microglia in 5xFAD mice expressing GFP exclusively in microglia. We found that over intervals of minutes to days, the microglial processes wrapping plaques were highly stable in contrast to the motile processes in the same cells that were not contacting plaques (Fig. 1c–g and Supplementary Movie 1). However, when we monitored the same individual plaques and microglia over intervals of months, we observed some rearrangement of the microglia processes contacting plaques, with an overall significant reduction in the degree of coverage (Fig. 1e–g), consistent with our data from fixed tissues showing that the degree of microglial coverage is lower as plaques grow in size (Fig. 1b).

Given the tight and stable contact between microglia processes with the plaque surface[22], we asked whether this interaction was capable of restricting the binding of interstitial soluble Aβ to the plaque. We performed *in vivo* two photon imaging of fibrillar amyloid plaques pre-labeled with the fluorescent fibrillar amyloid-binding dye FSB, while simultaneously microinjecting fluorescently-conjugated soluble Aβ40-555 or Aβ42-555 into the subarachnoid space (Fig. 2a–b). Within minutes of injection, both Aβ40 and Aβ42 diffused throughout the hemisphere and rapidly bound with high-affinity to pre-existing FSB-labeled fibrillar plaques (Fig. 2c–e and Supplementary Movie 2). Thus, even among the most robustly enveloped amyloid plaques, microglia processes are not capable of preventing the diffusion of Aβ into the plaque core.

Soluble Aβ42 has a high affinity for plaque micro-regions with low fibrillar amyloid density

We then imaged plaques at higher-resolution after subarachnoid Aβ-555 infusion and were surprised to observe a striking difference between Aβ40 and Aβ42. Aβ42-555 showed a very heterogeneous binding pattern with hotspots of markedly increased affinity (Fig. 2f), while Aβ40-555 binding was more homogeneous throughout the plaque (Fig. 2f–g, Supplementary Fig. 1a). The dramatic discrepancy in binding patterns is unlikely to be due to differential diffusion properties of Aβ40 and Aβ42 given their similar molecular size and the fact that an identical pattern of Aβ42 hotspot binding was observed after directly exposing plaques to Aβ42 in either unfixed freshly cut or fixed and permeabilized brain slices (Fig. 3a–b). Furthermore, a scrambled Aβ42 peptide did not bind to plaques at all (Supplementary Fig. 1c). Importantly, immunohistochemistry on fixed brain slices with c-terminal specific antibodies demonstrated that endogenous Aβ42 also accumulates in these hotspot microregions (Fig. 3c). This strongly suggests that plaque micro-regions have distinct biochemical conformations that cause the differential and specific Aβ42 affinities leading to the observed hotspots.

We further examined the intrinsic differences between plaque micro-regions with or without Aβ42-555 hotspots (Fig 4a). We found that Aβ42 hotspots invariably co-localized with regions containing low fibrillar amyloid density, as evidenced by the inverse relationship between Aβ42 and Thioflavin S (TS) fluorescence intensities (Fig. 4b–e). Furthermore, non-

hotspot areas were characterized by a more distinct TS-labelled fibrillar plaque edge, compared to the gradual tapering of TS labelling near Aβ42 hotspots (Fig. 4f–h). This indicates that the presence of preexisting amyloid fibrils is critical for soluble Aβ42 binding to occur, but as the amyloid plaque becomes gradually denser and compact, the affinity for new soluble Aβ42 is dramatically reduced.

Aβ42 hotspots are anti-colocalized with microglia processes

Given the incomplete plaque coverage by microglia (Fig. 1), we next explored the possibility that the patchy fibrillar plaque affinity for soluble Aβ42 is influenced by the presence of microglia processes. To examine this, we obtained high-resolution confocal images of microglia around plaques and correlated their location with the presence of Aβ42-555 hot-spots and the relative density of fibrillar amyloid (TS fluorescence). We found that plaque surface regions not covered by microglia processes had a much lower TS fluorescence intensity (Supplementary Fig. 3) but exhibited strong Aβ42-555 labeling, while immediately adjacent regions wrapped by microglia processes had greater TS fluorescence but much less Aβ42-555 labeling (Fig 5a–c). Furthermore, smaller plaques, which tended to be completely wrapped by microglia processes and had minimal Aβ42 binding, while larger plaques were less covered by microglia but showed high-affinity Aβ42 binding (Fig. 5d,e).

In contrast to microglia, the location of reactive astrocytes, which also have polarized processes making extensive contact with the plaque surface, did not show any spatial correlation with TS or Aβ42-555 fluorescence (Fig. 5f,g and Supplementary Fig. 5). Thus, these data strongly suggest that the presence of microglial processes is a critical determinant of the degree of amyloid compaction, which markedly affects the affinity of plaques to soluble Aβ42.

Protofibrillar Aβ42 hotspots can be revealed with specific Aβ binding dyes

Given our findings that plaque micro-regions with low levels of amyloid compaction in microglia-uncovered areas have a much greater affinity for exogenous Aβ42-555, we hypothesized that these areas would also be sites of active binding and polymerization of endogenously produced Aβ. However, endogenous forms of protofibrillar Aβ are difficult to visualize in intact tissues because of a lack of specific antibodies for these Aβ conformations. Instead, we tested the properties of a variety of fluorescent small molecule dyes known to have affinity for amyloid plaques. We found that like Thioflavin-S, the majority of Congo red and Thioflavin-T derivatives mainly bind to the fibrillar plaque core (Fig. 6c–h). Surprisingly, the natural product Curcumin[33] and the synthetic compound THK-265[34] both displayed a unique binding pattern remarkably similar to that of exogenously infused Aβ42 (Fig. 6a,b,i and Supplementary Fig. 1e). Curcumin has been shown *in vitro* to bind oligomeric and protofibrillar Aβ[33,35]. To determine whether Curcumin and THK-265 are binding to oligomeric Aβ enriched in these hotspots, we immunolabeled brain slices with the oligomer-specific antibodies A11 and OC[36,37]. These antibodies, however, did not show any hotspot pattern, but instead labeled the plaque perimeters uniformly as well as small puncta throughout the brain parenchyma (Supplementary Fig. 2) suggesting that hotspots are not enriched in Aβ oligomers. The fact that the labeling by Curcumin and THK-265 but not Thioflavin S is highly colocalized with

that of infused Aβ42-555 and endogenous Aβ42 immunolabeling (Fig. 3C), strongly suggests that hotspots are sites of active aggregation for endogenous Aβ42 into protofibrils.

These data demonstrate that the protofibrillar Aβ42 hot-spots are determined by intrinsic biochemical differences within plaque micro-regions that can be unambiguously revealed *in vivo* by fluorescently-labeled Aβ42 or specific Aβ binding dyes.

Neuritic dystrophy is more severe next to plaque regions lacking microglia processes

Oligomeric and protofibrillar forms of Aβ have been shown to be significantly more neurotoxic than larger Aβ aggregates [38,39]. Given our finding that plaque micro-regions not covered by microglia, are hot-spots rich in protofibrillar Aβ42, we asked whether these regions were associated with greater axonal dystrophy than the adjacent ones that were covered by microglia processes. To address this question, we first performed immunolabeling of dystrophic neurites using anti-Lamp1 or anti-Ubiquitin antibodies, which robustly demarcate the swollen dystrophic axons around fibrillar amyloid plaques as previously shown by confocal[40] and electron microscopy[41–43](Fig. 7a–d). Quantitative confocal microscopy revealed that plaque regions covered by microglia had significantly fewer dystrophic neurites than those without microglia processes (Fig 7b,d). We then examined the dynamics of dystrophic neurite formation and elimination by *in vivo* two photon imaging and correlated it with the location of microglia processes. We used a triple transgenic strategy by crossbreeding 5xFAD mice with mice expressing GFP in microglia (*CX3CR1*[GFP/+]), while neurons were labeled by further crossbreeding with mice expressing YFP under the Thy1 promoter or by cortical infection with an adeno-associated virus driving neuronal expression of tdTomato. We found that areas not covered by microglia had an even greater degree of axonal dystrophy than microglia-covered areas compared to what was apparent by anti-Lamp1 or anti-Ubiquitin immunolabeling (Fig. 7e,f). Furthermore, time-lapse *in vivo* imaging showed a markedly increased rate of dystrophic neurite formation in areas lacking microglia processes (Fig. 7g,h), supporting the concept of increased neurotoxicity by protofibrillar Aβ42 hot-spots.

Taken together, these data demonstrate that plaque areas without microglia processes are sites of greater neurotoxicity likely due to the accumulation of endogenous protofibrillar Aβ42. Furthermore, it suggests that microglia act as a barrier that shields neurons from the local toxicity associated with the ongoing aggregation of Aβ.

The neuroprotective barrier provided by microglia declines in aging

To explore the effects of aging on the ability of microglia to form an effective barrier, we compared the number of microglia and their degree of coverage of the plaque surface across different ages. We found that as mice became older there was a gradual decrease in the average number of microglia within a 25 μm radius of the plaque perimeter (Fig. 8a), which was at least partly due to a diminished proliferative capacity (Fig. 8b). This reduction led to a significant difference in the degree of microglia process envelopment of the plaque surface (Fig. 8a). We then probed whether this microglia reduction had any effect on the degree of Aβ aggregation and toxicity around plaques. We first looked at the amount of protofibrillar Aβ42 by measuring the perimeter of curcumin labeling around plaques of various sizes and

at different mouse ages. Interestingly, we found that in 18 to 24 month-old CRND8 mice, plaques of equivalent size as in 4 month-old mice had a markedly increased protofibrillar Aβ42 halo (Fig. 8c,e). Furthermore, the accumulation of protofibrillar Aβ was associated with a large increase in the area of dystrophic neurites (Fig. 8d,f). These data demonstrate that microglia aging is associated with a profound increase in the accumulation of protofibrillar Aβ around plaques and in worsened neuritic pathology, which could be partly due to an ineffective microglia barrier function.

Modulation of the microglia barrier ameliorates plaque neurotoxicity

Given our evidence of greater dystrophic neuropathology near plaque micro-regions lacking microglia coverage and in aged mice with fewer microglia around plaques, we hypothesized that enhancing microglia coverage would have a neuroprotective effect. We have previously shown that microglia clustering around individual plaques can be manipulated by deletion of the chemokine receptor *CX3CR1*[19]. We thus crossbred CRND8 with *CX3CR1*^{−/−} mice and showed that CRND8/*CX3CR1*^{−/−} mice had an increase in microglia process coverage of individual amyloid plaques (Fig 9a,b). Furthermore, quantification of dystrophic neurites demonstrated that increased microglia process coverage in CRND8/*CX3CR1*^{−/−} mice was associated with a significant reduction in neuritic dystrophy (Fig 9c). A similar reduction in neuritic dystrophy following *CX3CR1* knockdown was observed in another Aβ amyloidosis mouse model (5xFAD) (Supplementary Fig. 6). Interestingly, despite the fact that microglia coverage was increased in plaques of all sizes, we only observed reduced neuritic dystrophy in relatively small plaques, while larger ones, which are likely to be older[40], had the same degree of dystrophy regardless of *CX3CR1* genotype (Fig. 9c).

We also tested passive anti-Aβ immunization as a method to enhance microglia process coverage given that anti-Aβ antibodies have been shown to induce microglia activation around plaques[29,30]. Indeed, administration of AB9 antibody to young 5xFAD mice over 8 weeks induced a marked increase of microglia process coverage of fibrillar plaques (Fig. 9d). Similar to mice lacking *CX3CR1*, the neuroprotective effect of increased microglia coverage was mainly observed in smaller plaques which are likely to be the newest ones[40](Fig. 9e,f).

Taken together, we demonstrate that molecular manipulation of microglia can promote the barrier phenotype which preferentially reduces local neurotoxicity around small early-stage plaques, suggesting that microglial processes wrapping the plaque core actively protect adjacent neurons from Aβ toxicity within a critical period during plaque development.

DISCUSSION

We uncovered a previously unrecognized function of microglia in Alzheimer's disease which could be critical in the progression of amyloid deposition and its associated neurotoxicity. Our findings provide a framework for a better understanding of the role of microglia in neurodegeneration, which has gained significant importance as a result of evidence of genetic variants in microglia-related genes that increase the risk of late onset AD[8–12].

Our data supports a model in which microglia envelopment of amyloid plaques acts as a barrier that plays a critical role in modulating the degree of plaque compaction, a key factor in determining the ongoing affinity of plaques for soluble Aβ42 binding and consequent formation of protofibrillar Aβ42 hot-spots. Several mechanisms could contribute to the microglia barrier function (Supplementary Fig. 9). The close physical proximity of microglia processes which are intertwined with the growing amyloid fibrils[21,22] could act as a physical barrier that restricts their polymerization. Microglia processes create a crowded microenvironment that could prevent the normal outward elongation of the fibrils by promoting their bending or compaction[44]. In this scenario, microglia may insulate the growing fibril tips from recruiting interstitial soluble Aβ by promoting the formation of fibril conformers with reduced Aβ affinity[45,46]. The location of this physical barrier is relatively stable over months given the minimal motility of microglia process contacting the plaque compared to the highly motile processes away from plaques (Fig. 1). Nevertheless, our fluorescent Aβ42 sequential infusion over 60 days (Supplementary Fig. 4) demonstrates a gradual shift in the hotspot location, likely due to rearrangement of microglia processes. In addition to a physical cellular barrier, active microglia phagocytosis of oligomeric Aβ[19,47] and proteolytic activity by microglial secreted enzymes[48,49] could further reduce local polymerization and prevent fibril extension.

The remarkable affinity to areas not covered by microglia processes of certain Aβ-binding dyes known to bind to protofibrillar Aβ, such as Curcumin[33,35] and THK-265, as well as exogenous soluble Aβ42, strongly support the concept that microglia-uncovered areas are hot-spots of active Aβ polymerization. The minimal Thioflavin-positive fibrils present in the hotspot region, is consistent with *in vitro* data demonstrating that low amounts of fibrils are necessary to efficiently polymerize oligomers and protofibrils from soluble monomers[50]. The fact that these small molecular weight dyes have very different binding properties compared to similarly sized Aβ-binding dyes derived from Congo-red or Thioflavin-T (Fig. 6), suggests that the high affinity for plaque areas of less compact amyloid in microglia-uncovered regions, is not due to differences in molecular size of the ligand but rather specific biochemical affinities due to Aβ conformations. A similar phenomenon could explain the marked difference in the patterns of binding observed between Aβ40 and Aβ42.

Currently, FDA approved amyloid binding positron emission tomography (PET) tracers used in patients with suspected AD, are derived from Thioflavin-T[51] and Stilbene[52], which predominantly bind to the fibrillar plaque core and have negligible affinity for the protofibrillar Aβ42 around plaques. This could explain the poor correlation observed between PET signal and the degree of cognitive dysfunction when using these compounds for clinical imaging. The observation of a markedly greater protofibrillar Aβ halo and degree of neuritic dystrophy around fibrillar plaques of equal size when comparing young adults with aging transgenic mice (Fig. 8) further highlights the limitations of using PET tracers with affinity to the plaque core. Our observation that the most toxic plaque areas are those that contain protofibrillar Aβ42 hotspots in microglia uncovered-regions, suggests that PET ligands with affinity to these areas could have a much greater specificity for clinical AD diagnosis and staging. Furthermore, similar molecules with specific affinity for the

protofibrillar Aβ42 hotspots could be better at disrupting Aβ polymerization[53,54] than those that target the plaque core and may thus have greater therapeutic potential.

Our findings that the overall degree of dystrophy around plaques is inversely correlated with the extent of microglia plaque envelopment, that areas covered by microglia processes have fewer dystrophic neurites and a lower rate of dystrophic neurite formation and that *CX3CR1* knockdown and anti-Aβ immunotherapy reduce dystrophic neurites, strongly suggest that microglia exert a neuroprotective effect (Supplementary discussion). Microglia, could act as a physical barrier that insulates plaques from their surrounding neurites, reducing their contact with potentially damaging Aβ protofibrils[55,56]. In addition, it has been shown in vitro that an increased ratio of Aβ42 to Aβ40 increases neurotoxicity[57–59]. This is consistent with our in vivo findings of hotspots of Aβ42 that colocalize with greater neuritic dystrophy. Furthermore, the active process of Aβ polymerization by itself could be more toxic than the static presence of fibrils[38,60]. Thus by creating a microenvironment that is not favorable to ongoing Aβ42 polymerization, microglia could limit damage to adjacent neurites.

The role of microglia is further highlighted by our findings that in aging, the decline in microglia proliferation[61] leads to a reduction in microglia numbers and degree of envelopment of amyloid plaques, which is associated with a dramatic increase in the size of the protofibrillar Aβ halo and in the number of dystrophic neurites. Thus, while microglia could cause secondary neurotoxicity due to their ability to secrete cytokines and reactive oxygen species[31]; it appears that in the vicinity of amyloid plaques where they can modulate the degree of amyloid compaction, they exert a net protective effect. Our observations could provide a mechanistic explanation for the increased plaque compaction and reduced neurotoxicity recently observed after manipulating IGF-1 signaling in AD mice[62]. It could also explain why despite equivalent fibrillar plaque load, greater oligomeric Aβ concentrations are predictive of worse cognitive status in human patients[63].

Interestingly, we found that microglia envelopment was most effective at limiting protofibrillar Aβ accumulation and neuritic dystrophy around smaller plaques, even after *CX3CR1* chemokine receptor deletion or anti-Aβ immunotherapy. This suggests that the importance of the microglia barrier is most prominent at the initial stages of fibrillar amyloid deposition and becomes less effective as plaques grow in size. This could explain why recent studies of microglia ablation in advanced stages of amyloidosis did not demonstrate any effect on plaque counts or neuritic dystrophy[64].

To what extent the microglia barrier plays a role in human Alzheimer's disease remains to be determined. Given that in sporadic AD, the process of amyloid deposition is likely to be much slower than in transgenic models, it is possible that in human sporadic and familial AD, the microglia barrier would have unique spatial-temporal properties. Nevertheless, therapeutic interventions targeted at the microglia barrier may be most effective at early stages of plaque evolution. However, the modest reduction of dystrophic neurites that we observed after anti-Aβ immunotherapy, despite a robust increase in the microglia envelopment, suggests that immunotherapy could have detrimental effects that counteract the beneficial effects of the microglia barrier. This could partly explain the failure of such

therapeutic approach in clinical trials[27], and suggests that a more specific strategy to enhance the microglia barrier may offer more effective neuroprotection.

Together, our results demonstrate that microglia envelopment of amyloid plaques in AD is a highly coordinated process aimed at increasing the degree of compaction of fibrillar amyloid deposits while limiting the accumulation of potentially neurotoxic protofibrillar Aβ aggregates and shielding neurons from them. Understanding the precise mechanisms involved in this newly identified microglial function may further elucidate their neuroprotective role in AD and other neurodegenerative disorders.

METHODS

Transgenic mouse strains

All animal experimental procedures were performed in accordance with Federal and State regulations and approved by the Institutional Animal Care and Use Committee (IACUC) at Yale University and Northwestern University. Two AD mouse models were used in this study: CRND8 (Courtesy of Dr. David Westaway, University of Toronto) which harbors human APP695 with KM670/671/NL (Swedish) and V717F (Indiana) mutations driven by the Prion promoter; and 5XFAD (Courtesy of Dr. Robert Vassar, Northwestern University) which overexpresses both human APP695 with KM670/671/NL (Swedish), V717I (London) and I716V (Florida) mutations and human PS1 harboring M146L and L286V mutations under the Thy1 promoter. Heterozygous males were bred with C57Bl/6 females and litters were genotyped by PCR using the following primers: for CRND8 mice, 5′ primer: AGGACTGACCACTCGACCAG; 3′ primer: CGGGGGTCTAGTTCTGCAT. For 5xFAD mice, 5′ primer: AATAGAGAACGGCAGGAGCA; 3′ primer: GCCATGAGGGCACTAATCAT. Thy1-YFP mice were crossbred with AD mice, in order to visualize the dystrophic neurites around amyloid plaques in some experiments. To manipulate the *CX3CR1* gene, mice with the *CX3CR1* loci replaced by GFP (*CX3CR1* Knock-in, The Jackson Laboratory 005582) were crossbred with CRND8 mice. Combined age-matched litters (6-month-old unless otherwise indicated) were used for all experiments.

Reagents and Antibodies

Fluorescently labeled Aβ peptides were provided by Anaspec (Hylite Fluor™ 555-Aβ42 60480-1, Hylite Fluor™ 488 labeled scrambled Aβ42 25382, Biotin-LC-Aβ42 24641-01, Hylite Fluor™ 488-Aβ40 60491-01 and Hylite Fluor™ 555-Aβ40 60492-01). Lyophilized peptides were dissolved in DMSO in concentration of 1mg/ml and stored as stock. Anti-Iba1 polyclonal antibody (Wako, 019-19741) was used to label microglia. Anti-GFAP polyclonal antibody (Dako, Z0334) was used to label astrocytes. Anti-Lamp1 (DSHB, 1D4B) and anti-Ubiquitin monoclonal antibody (Cell Signaling, 3936) were used to label dystrophic neurites. C-terminal specific antibodies for Aβ42 (Life technologies, 700254 and BioLegend, SIG39142-200) and Aβ40 (Millipore, AB5074P) were used for labeling amyloid plaques. 4G8 (BioLegend, SIG-39200), and MOAB-2 (Biosensis, M-1586-100), antibodies were used for labeling other Aβ fragments in the brain. Aβ conformation specific antibodies, A11 (Life Technologies, AHB0052) and OC (Millipore, AB2286), were used for labeling oligomeric Aβ. AlexaFluor-conjugated IgGs were used as secondary antibodies (Life

technologies). Small molecule Aβ binding dyes used in the study are: FSB (Santa Cruz, sc-359845), Thioflavin S (Sigma-Aldrich, T1892), Thioflavin T (Sigma-Aldrich, T3516), Congo red (Sigma-Aldrich C6277), Thiazine red (MP Biochemicals, 05208297), Methoxy-X04 (gift from W. Klunk), BTA-1 (Sigma Aldrich, B9934), Curcumin (Sigma-Aldrich, 08511) and THK-265 (Sigma-Aldrich, R277002).

Recombinant adeno-associated virus (AAV) production

DNA sequence of tdTomato fluorescent protein was ligated between the ITR sites of an AAV packaging plasmid with CAG promoter and WPRE/SV40 sequence. HEK293T cells were co-transfected with this construct and a helper plasmid pDP2 (PlasmidFactory, #PF402) for 96 hours and harvested. Virus was purified through iodixanol density centrifugation and titrated by infecting HEK293T cells.

In vivo Aβ42 brain infusion via subarachnoid space

Aβ peptide was injected into the mouse subarachnoid space as previously described[19]. In brief: mice were anesthetized with Ketamine-Xylazine, a thin-skull window about 1mm in diameter was made with a dental drill at 5.0mm antero-posterior, 2.5mm mediolateral from bregma. A ~300μm × 300μm piece of skull was lifted with a 25G needle to expose the tissue underneath, and the dura was carefully removed without touching the brain parenchyma. Aβ peptide was diluted in fresh sterile ACSF (1:9 v/v) at 37° C for 10 min before placing on ice. The solution filled a Tygon tube connected to a polypropylene tip with an outer diameter of 70μm. A programmable syringe pump with a Hamilton syringe was connected to the tube. The tip was then inserted into the exposed subarachnoid space and fixed with cyanoacrylate glue. 10μl of Aβ solution was injected at speed of 0.2μl/min. After injection, the tip was removed and mouse scalp was sutured. Mice were put on a heating pad for recovery and received Buprenex analgesia. At various time points after injection, mice were either imaged *in vivo* with two-photon microscopy or sacrificed for fixed tissue confocal imaging.

Fresh brain slice Aβ labeling

Mice were decapitated under anesthesia. Brains were dissociated on cooled ACSF with continuous oxygenation. After dissociation, brains were immediately transferred onto a vibratome. Coronal sections were made at 150μm thickness. Fluorescently labeled Aβ42 was added into the incubation bath to make a final concentration of 2μg/ml. Slices were incubated on a shaker for 1h at 4 °C and then washed twice with ACSF. After the last wash, slices were fixed in 4% paraformaldehyde at room temperature for 1h. Fixed slices were then washed with PBS before imaging.

Fixed brain slice Aβ labeling

Fixed brain slices were washed three times with PBS, then incubated at 95 °C for 30 min (Buffer: 10mM sodium citrate, 0.05% Tween 20 (v/v)). Slices were further washed in PBS with 0.2% TritonX-100 before adding fluorescently labeled Aβ to a final concentration of 5μg/ml. Slices were incubated at 4 °C on a shaker for 24h, and then washed three times in PBS before mounting for imaging.

Immunohistochemistry

Fixed brains were sectioned to 30μm thickness using a Leica vibratome (VT1000S). For Ubiquitin, sections underwent heat-induced antigen retrieval at 95 °C for 30min (Buffer: 10mM sodium citrate, 0.05% Tween 20 (v/v), pH=6.0). For Aβ-antibody staining, sections were pre-treated with an antigen retrieval buffer containing 70% formic acid in 1x PBS for 10 minutes and washed with 1x PBS. Primary antibodies were diluted in saline with 0.2% (v/v) Triton-X 100 and 4% (v/v) normal goat serum (Jackson ImmunoResearch 005-000-121). Sections were incubated with the primary antibody solution at 4 °C for two days followed by secondary antibodies for 5h. For amyloid plaque staining, a Thioflavin S solution (0.0003% (m/m)) was used for 15min incubation at RT. Stained sections were mounted onto glass slides with PermaFluor mounting medium (Thermo Scientific, TA-030-FM).

Quantitative analysis of Aβ42 hotspots in fixed brain slices

Aβ labeling was visualized with a Leica SP5 laser scanning confocal microscope with a Leica 63x oil objective (N.A 1.4). Images were taken with a standard step size of 0.7μm. Emission of Thioflavin S and fluorescently labeled Aβ were collected sequentially. All images were taken with a 512×512 pixel resolution and 8-bit color depth. All images were processed using custom-written ImageJ macros. A maximum intensity Z-projection of 5 optical slices through the center of the plaque was made to create a single image for analysis. Plaque area was determined by setting a threshold of three standard deviations above the entire image mean intensity. For analyzing the interface between plaque and hotspots, the selection of thresholded plaque area was enlarged 2μm radially outward in order to include the hotspot area. Fluorescence intensities in both channels were analyzed along a line between the center point of the plaque and each individual point in the perimeter of the enlarged selection. Fluorescent intensities were normalized to a 0–1 scale with the highest pixel intensity of the image as 1. To calculate the slope of fluorescent intensity change, a linear regression was fitted to the data set 10 points before and after the thresholded plaque border. To calculate the total fluorescence in the plaque halo (the area under the curve), sum of pixel intensities within the thresholded plaque border was used. Each line was categorized as hotspot or non-hotspot based on its maximum intensity in the Aβ42 channel and as microglia-covered or uncovered based on its microglia intensity (as in Supplementary Figure 3). For the purpose of display, each line was resampled into 50 points using "Array.resample" function in ImageJ.

Microglia coverage and dystrophic neurite quantification

Imaging conditions were the same as described above except for having three emission channels. Plaques were chosen from cortex, layer IV–VI. Images were numbered randomly and blinded for analysis. All images were processed with a customized ImageJ macro. Plaque area was identified by setting threshold for one standard deviation above the entire image mean intensity. 5 optical slices through the center of the plaque were used for analysis. On each slice, the intersection between the tips of microglia process and the plaque perimeter were identified manually. The proportion of the plaque perimeter covered by microglia processes was calculated by summing the arcs of plaque perimeter that

colocalized with microglia processes. Dystrophic neurite area was determined by setting a threshold for one standard deviation above the entire image mean intensity. The plaque area was excluded from this area quantification. In the experiment using Thy1-YFP mice, dystrophic neurites were counted manually. To compare the area with or without microglia coverage, the coverage angle was converted to a triangular selection. The selection was then extended to the limits of the image. The overlap between this extended selection and the dystrophic area was defined as the dystrophic area in the covered region of the plaque. Dystrophic neurite area was normalized per angular degrees of associated plaque perimeter. That is, the DN area was divided by the relative amount of the plaque covered or uncovered in angular degrees using the formulas below: 1) for microglia covered areas: Dystrophy/coverage=(area of dystrophic neurites outward of microglia covered plaque perimeter)/(degrees of arc of microglia coverage). 2) for microglia uncovered areas: Dystrophy/coverage= (total area of dystrophic neurites – covered portion of dystrophic neurite area)/(360-arc of microglia coverage). A similar analysis was used for comparing dystrophic neurites count, Aβ42 binding, curcumin and THK265 fluorescence. Plaques with diameter between 6 to 9 microns were used in these analyses. For each measurement, the average of results for 5 optical slices was reported as a measurement for individual plaque. Statistical analyses were performed in GraphPad Prism, using two-tailed T-test assuming same standard deviation.

In vivo two-photon time-lapse imaging of Aβ binding

Mice received FSB injection (I.P. 7.5mg/kg) two days prior to the experiment. In the experiments requiring astrocyte labeling, freshly-made sulforhodamine 101 solution (5mM, 100μL/mouse) was injected (I.V.) one day prior to the experiment. Mice were anesthetized with Ketamine-Xylazine, a thin-skull window about 2mm in diameter was made with a dental drill at 2.0mm antero-posterior, 3mm mediolateral from bregma. A 200μm × 200μm opening on the posterior side of the window was made with a 25G needle to expose the tissue underneath. And then the dura was carefully removed. Using a motorized manipulator (Sutter instrument, MP-285), a micro glass-pipette filled with Aβ peptide solution (described above) was inserted into the opening. The pipette was connected with a picospritzer microinjection system (Parker Hannifin Corporation, 051-0500-900) set at 30 psi. Infusion of Aβ solution was initiated by giving several 100ms pulses through the picospritzer.

In vivo two-photon imaging (Prairie technology) was performed with a Ti-Sapphire laser (Mai Tai Spectra Physics) with a 20x water immersion objective (Leica, NA 1.0). Time-lapse images were taken about 200μm away from the pipette tip. To increase the probability of capturing the binding process, XYZT stacks were taken from a 100μm (X, 512 pixel) × 100μm (Y, 512 pixel) × 50μm (Z, step size 3) volume. Each XYZ cycle took about 20s. Aβ42-555, Aβ42-488 and GFP fluorophores were excited at 925nm; FSB and sulforhodamine 101 were excited at 850 nm.

To analyze Aβ binding, images were first corrected for minor movement artifacts using "StackReg" plugin in Fiji (www.fiji.sc). Subsequently different channels were merged together using the "Merge Channels…" function. Each region for analysis was extracted from the original XYZT stack by making a 3 optical slices projection centered at the middle

plane of the amyloid plaque. In the projected XYT stacks, plaque regions were defined by thresholding the FSB channel (3 standard deviations from the mean). Microglia regions were defined by thresholding the GFP channel (1.5 standard deviations from the mean) and excluding the plaque regions. Aβ42 binding was reported as ratios of fluorescence intensity between red channels (Aβ42-555) and green channels (*CX3CR1*-GFP) in order to account for the change of focal plane.

Short-term in vivo two-photon imaging of microglia dynamism

Microglia were labeled by crossing CRND8 or 5xFAD mice with *CX3CR1*-GFP mice. 8–10 months old mice were used in these experiments. Mice were anesthetized with Ketamine-Xylazine, a craniotomy window about 2mm in diameter was made at 3.0mm antero-posterior, 3mm mediolateral from bregma. The Duramater was removed with a #7 tweezer (Dumont) avoiding bleeding or damage to the cortex. Topical application of thiazine red solution was used to label amyloid plaques for 30mins. A thin glass coverslip (#0) was pre-cut and fixed directly on the skull after the excess dye was washed-out. In vivo two photon microscopy imaging was performed. XYZT stacks were taken from a 200μm (X, 1024 pixel) × 200μm (Y, 1024 pixel) × 100μm (Z, step size 3) volume. GFP and Thiazine red were excited at 900nm. To analyze microglia process dynamism, images were first corrected for minor movement artifacts using "StackReg" plugin in Fiji. Each region for analysis was extracted from the original XYZT stack by making a 3 optical slice projection centered at the middle plane of the amyloid plaque. In the projected XYT stacks, plaque regions were defined by thresholding the FSB channel (3 standard deviations from the mean). Microglia regions were defined by thresholding the GFP channel (1.5 standard deviations from the mean). Dynamism was determined by calculating the overlap between the thresholded areas of microglia processes between the first time-point and later time-points.

Long-term in vivo two-photon imaging of microglia dynamism

Microglia were labeled by crossing CRND8 with *CX3CR1*-GFP mice. 10–12 months old mice were used in these experiments. Mice were injected with FSB (7.5mg/kg, I.P.) 2 days prior to each imaging session. In the first session, a thin-skull window about 2mm in diameter was made with a dental drill at 2.0mm antero-posterior, 3mm mediolateral from bregma. The window was polished before imaging in the subsequent sessions with a micro blade (Surgistar, 6961). A landmark picture was taken of the surface pial vessels. All coordinates of imaging regions relative to the landmark location were recorded. In later imaging sessions, relocation was achieved by matching the landmark blood vessel shape and orientations to the original landmark picture, and then reloading the coordinates. In each plaque region, a XYZ stacks were taken from a 150μm (X, 1024 pixel) × 150μm (Y, 1024 pixel) × 30μm (Z, step size 1) volume. GFP was excited with 950nm laser and FSB was excited with 850nm laser. To analyze microglia process dynamism, GFP and FSB channels were first merged together using the "Merge Channels…" function. Each region for analysis was extracted from the original XYZ stack by making a 3 optical slices projection centered at the middle plane of the amyloid plaque. The projected images from the same location at different time-points were aligned manually based on maximizing the overlap of the plaque center, microglia cell bodies and lipofuscin granules. After alignment, pictures from the same location were compiled into a single stack. In each slice of the stack, plaque regions

were defined by thresholding the FSB channel (3 standard deviations from the mean). The intersection between the tips of microglia process and the plaque perimeter were identified manually. The plaque perimeter was divided into 360 degrees based on the angle from the plaque center and coverage was calculated using the summed degrees of plaque perimeter arcs that colocalized with microglia processes. These coverage data was recorded as a 360 length binary array for each time point. In all time series the first imaging session was used as the reference and designated as "day0". Stable processes were calculated by multiplying the array from day0 to day1, 5, 10 and 50. Added processes were calculated by subtracting the stable processes from day1, 5, 10 and 50's arrays.

In vivo two-photon imaging of dystrophic neurite turnover

CRND8 and 5xFAD mice were crossbred with *CX3CR1-GFP* mice to visualize microglia. In order to label dystrophic neurites the mice were either further crossbred with Thy1-YFP mice or injected with AAV-tdTomato virus through the subarachnoid space as described above. Mice were injected with FSB, I.P. (7.5mg/kg) 1 day prior to the first imaging session to label amyloid plaques. Mice were anesthetized with Ketamine/Xylazine. A thinned-skull window ~500μm in diameter was made at −2 mm to Bregma and 2.5mm lateral to the midline. In vivo two-photon imaging was performed as described above. Amyloid plaques were identified within 150μm of the pial surface. Individual amyloid plaques were imaged with 825nm excitation for FSB and 950nm excitation for both microglia (GFP) and DNs (YFP or tdTomato). Image stacks were taken for each plaque at 1μm step size. Plaque location was recorded and each plaque was relocated 5 days later and imaged under the same conditions. For analysis, a maximum intensity Z-projection of 3 optical slices at the plaque center was made. Microglia coverage was determined as described above. Dystrophic neurite (DN) formation and elimination events were identified based on appearance or disappearance of DN in the second time point. Events were counted manually and categorized based on their proximity to microglia covered and uncovered plaque areas. The probability of elimination was calculated as the number of elimination events/number of pre-existing dystrophic neurites. The probability of formation was calculated as the number of events in microglia covered or uncovered regions/arc in degrees of microglia covered or uncovered plaque perimeter.

Passive immunization treatment

Ab9 administration was done as previously described[30]. In brief, 6 week old 5xFAD mice were randomly divided into three groups. One group received no injection. The second group received intraperitoneal injection of 1mg/ml mouse control IgG every two weeks. The third group received intraperitoneal injection of 1mg/ml Ab9 antibody every two weeks. 1 week after the fourth injection, mice were sacrificed and brains collected for quantitative immunohistochemistry.

Statistics

Data are represented as mean ± s.e.m. Histogram plots were used to observe approximate Gaussian distributions, upon which two-tail unpaired Student's t-tests were employed for comparisons between two groups. A probability of $p<0.05$ was considered indicative of

significant differences between groups. Data was additionally normalized to the average value of the measurements in the control group for better scaling of the result. In the experiments with *CX3CR1* gene knock out and Aβ passive immunization, we report statistical comparisons using both plaque numbers (Fig. 9) and animal numbers (Supplementary Fig. 7). Regardless of the method used, the results are equivalent in magnitude and statistically significant.

Supplementary Material

Refer to Web version on PubMed Central for supplementary material.
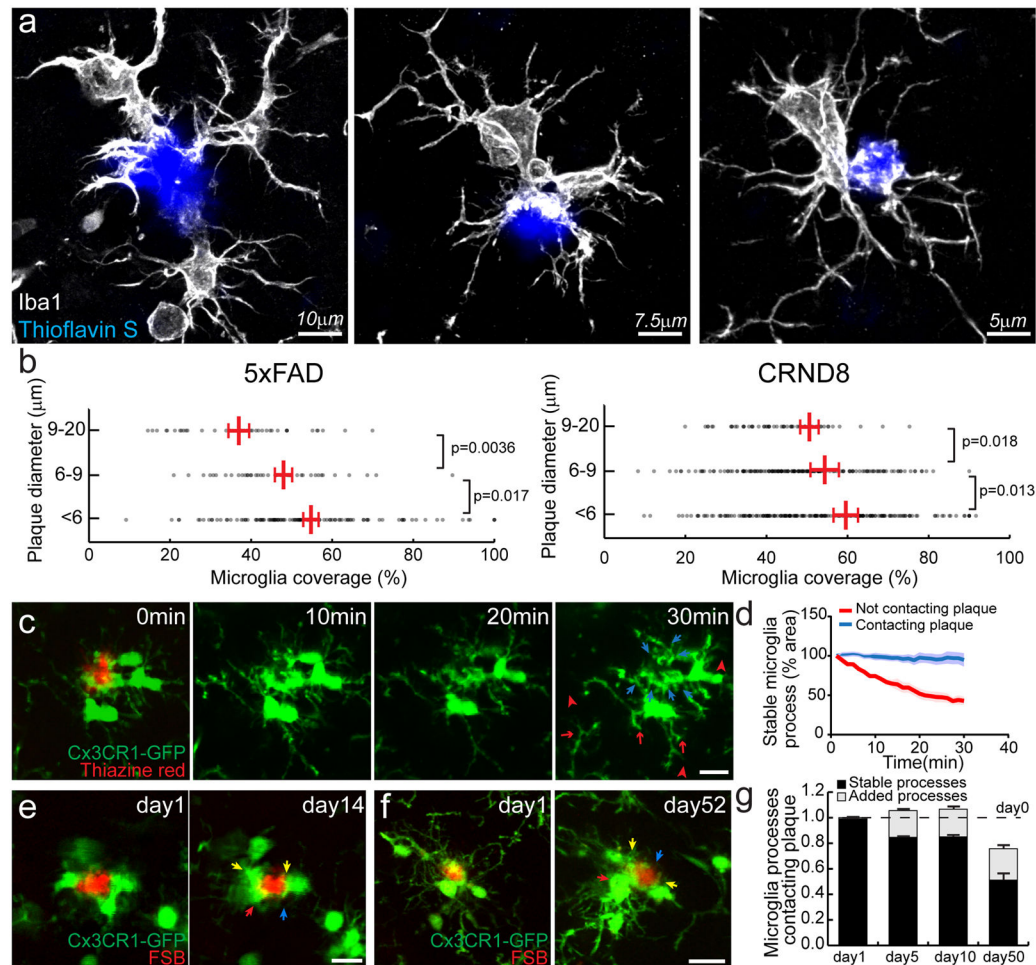
Acknowledgments

References

1. Bertram L, Lill CM, Tanzi RE. The genetics of Alzheimer disease: back to the future. Neuron. 2010; 68:270–81. [PubMed: 20955934]

2. Masters CL, Selkoe DJ. Biochemistry of amyloid β-protein and amyloid deposits in Alzheimer disease. Cold Spring Harb Perspect Med. 2012; 2:a006262. [PubMed: 22675658]

3. Palop JJ, Chin J, Mucke L. A network dysfunction perspective on neurodegenerative diseases. Nature. 2006; 443:768–73. [PubMed: 17051202]

4. Kim J, Basak JM, Holtzman DM. The role of apolipoprotein E in Alzheimer's disease. Neuron. 2009; 63:287–303. [PubMed: 19679070]

5. Iadecola C. The pathobiology of vascular dementia. Neuron. 2013; 80:844–66. [PubMed: 24267647]

6. Zlokovic BV. The blood-brain barrier in health and chronic neurodegenerative disorders. Neuron. 2008; 57:178–201. [PubMed: 18215617]

7. Mandrekar S, et al. Microglia mediate the clearance of soluble Abeta through fluid phase macropinocytosis. J Neurosci. 2009; 29:4252–62. [PubMed: 19339619]

8. Guerreiro R, et al. TREM2 variants in Alzheimer's disease. N Engl J Med. 2013; 368:117–27. [PubMed: 23150934]

9. Jonsson T, et al. Variant of TREM2 associated with the risk of Alzheimer's disease. N Engl J Med. 2013; 368:107–16. [PubMed: 23150908]

10. Ruiz A, et al. Assessing the role of the TREM2 p.R47H variant as a risk factor for Alzheimer's disease and frontotemporal dementia. Neurobiol Aging. 2013

11. Griciuc A, et al. Alzheimer's Disease Risk Gene CD33 Inhibits Microglial Uptake of Amyloid Beta. Neuron. 2013; 78:631–643. [PubMed: 23623698]

12. Bradshaw EM, et al. CD33 Alzheimer's disease locus: altered monocyte function and amyloid biology. Nat Neurosci. 2013

13. Davalos D, et al. ATP mediates rapid microglial response to local brain injury in vivo. Nat Neurosci. 2005; 8:752–8. [PubMed: 15895084]

14. Hanisch UK, Kettenmann H. Microglia: active sensor and versatile effector cells in the normal and pathologic brain. Nat Neurosci. 2007; 10:1387–94. [PubMed: 17965659]

15. Tsai J, Grutzendler J, Duff K, Gan WB. Fibrillar amyloid deposition leads to local synaptic abnormalities and breakage of neuronal branches. Nat Neurosci. 2004; 7:1181–3. [PubMed: 15475950]

16. Nagele RG, et al. Contribution of glial cells to the development of amyloid plaques in Alzheimer's disease. Neurobiol Aging. 25:663–74. [PubMed: 15172746]

17. Hickman SE, Allison EK, El Khoury J. Microglial dysfunction and defective beta-amyloid clearance pathways in aging Alzheimer's disease mice. J Neurosci. 2008; 28:8354–60. [PubMed: 18701698]

18. Maier M, et al. Complement C3 deficiency leads to accelerated amyloid beta plaque deposition and neurodegeneration and modulation of the microglia/macrophage phenotype in amyloid precursor protein transgenic mice. J Neurosci. 2008; 28:6333–41. [PubMed: 18562603]

19. Liu Z, Condello C, Schain A, Harb R, Grutzendler J. CX3CR1 in microglia regulates brain amyloid deposition through selective protofibrillar amyloid-β phagocytosis. J Neurosci. 2010; 30:17091–101. [PubMed: 21159979]

20. ITAGAKI S, MCGEER P, AKIYAMA H, ZHU S, SELKOE D. Relationship of microglia and astrocytes to amyloid deposits of Alzheimer disease. J Neuroimmunol. 1989; 24:173–182. [PubMed: 2808689]

21. Wegiel J, Wisniewski HM. The complex of microglial cells and amyloid star in three-dimensional reconstruction. Acta Neuropathol. 1990; 81:116–24. [PubMed: 2082651]

22. Stalder M, Deller T, Staufenbiel M, Jucker M. 3D-Reconstruction of microglia and amyloid in APP23 transgenic mice: no evidence of intracellular amyloid. Neurobiol Aging. 22:427–34. [PubMed: 11378249]

23. El Khoury J, et al. Ccr2 deficiency impairs microglial accumulation and accelerates progression of Alzheimer-like disease. Nat Med. 2007; 13:432–8. [PubMed: 17351623]

24. Naert G, Rivest S. CC chemokine receptor 2 deficiency aggravates cognitive impairments and amyloid pathology in a transgenic mouse model of Alzheimer's disease. J Neurosci. 2011; 31:6208–20. [PubMed: 21508244]

25. Zhu Y, et al. CD45 deficiency drives amyloid-β peptide oligomers and neuronal loss in Alzheimer's disease mice. J Neurosci. 2011; 31:1355–65. [PubMed: 21273420]

26. Song M, et al. TLR4 mutation reduces microglial activation, increases Abeta deposits and exacerbates cognitive deficits in a mouse model of Alzheimer's disease. J Neuroinflammation. 2011; 8:92. [PubMed: 21827663]

27. Lemere CA, Masliah E. Can Alzheimer disease be prevented by amyloid-beta immunotherapy? Nat Rev Neurol. 2010; 6:108–19. [PubMed: 20140000]

28. Wilcock DM, et al. Passive immunotherapy against Abeta in aged APP-transgenic mice reverses cognitive deficits and depletes parenchymal amyloid deposits in spite of increased vascular amyloid and microhemorrhage. J Neuroinflammation. 2004; 1:24. [PubMed: 15588287]

29. Levites Y, et al. Anti-Abeta42- and anti-Abeta40-specific mAbs attenuate amyloid deposition in an Alzheimer disease mouse model. J Clin Invest. 2006; 116:193–201. [PubMed: 16341263]

30. Wang A, Das P, Switzer RC, Golde TE, Jankowsky JL. Robust amyloid clearance in a mouse model of Alzheimer's disease provides novel insights into the mechanism of amyloid-beta immunotherapy. J Neurosci. 2011; 31:4124–36. [PubMed: 21411653]

31. McGeer EG, McGeer PL. Neuroinflammation in Alzheimer's disease and mild cognitive impairment: a field in its infancy. J Alzheimers Dis. 2010; 19:355–61. [PubMed: 20061650]

32. Gandy S, Heppner FL. Microglia as dynamic and essential components of the amyloid hypothesis. Neuron. 2013; 78:575–7. [PubMed: 23719156]

33. Yang F, et al. Curcumin inhibits formation of amyloid beta oligomers and fibrils, binds plaques, and reduces amyloid in vivo. J Biol Chem. 2005; 280:5892–901. [PubMed: 15590663]

34. Okamura N, et al. In vivo detection of amyloid plaques in the mouse brain using the near-infrared fluorescence probe THK-265. J Alzheimers Dis. 2011; 23:37–48. [PubMed: 20930313]

35. Yanagisawa D, et al. Curcuminoid binds to amyloid-β1-42 oligomer and fibril. J Alzheimers Dis. 2011; 24 (Suppl 2):33–42. [PubMed: 21335654]

36. Kayed R, et al. Fibril specific, conformation dependent antibodies recognize a generic epitope common to amyloid fibrils and fibrillar oligomers that is absent in prefibrillar oligomers. Mol Neurodegener. 2007; 2:18. [PubMed: 17897471]

37. Kayed R, et al. Conformation dependent monoclonal antibodies distinguish different replicating strains or conformers of prefibrillar Aβ oligomers. Mol Neurodegener. 2010; 5:57. [PubMed: 21144050]

38. Wogulis M, et al. Nucleation-dependent polymerization is an essential component of amyloid-mediated neuronal cell death. J Neurosci. 2005; 25:1071–80. [PubMed: 15689542]

39. O'Nuallain B, et al. Amyloid -Protein Dimers Rapidly Form Stable Synaptotoxic Protofibrils. J Neurosci. 2010; 30:14411–14419. [PubMed: 20980598]

40. Condello C, Schain A, Grutzendler J. Multicolor time-stamp reveals the dynamics and toxicity of amyloid deposition. Sci Rep. 2011

41. Nixon RA, et al. The lysosomal system in neurons. Involvement at multiple stages of Alzheimer's disease pathogenesis. Ann N Y Acad Sci. 1992; 674:65–88. [PubMed: 1288372]

42. Nixon RA, et al. Extensive involvement of autophagy in Alzheimer disease: an immuno-electron microscopy study. J Neuropathol Exp Neurol. 2005; 64:113–22. [PubMed: 15751225]

43. Sanchez-Varo R, et al. Abnormal accumulation of autophagic vesicles correlates with axonal and synaptic pathology in young Alzheimer's mice hippocampus. Acta Neuropathol. 2012; 123:53–70. [PubMed: 22020633]

44. Zhou Z, et al. Crowded cell-like environment accelerates the nucleation step of amyloidogenic protein misfolding. J Biol Chem. 2009; 284:30148–58. [PubMed: 19748895]

45. Ban T, Yamaguchi K, Goto Y. Direct observation of amyloid fibril growth, propagation, and adaptation. Acc Chem Res. 2006; 39:663–70. [PubMed: 16981683]

46. Jansen R, Grudzielanek S, Dzwolak W, Winter R. High pressure promotes circularly shaped insulin amyloid. J Mol Biol. 2004; 338:203–6. [PubMed: 15066425]

47. Mandrekar S, et al. Microglia mediate the clearance of soluble Abeta through fluid phase macropinocytosis. J Neurosci. 2009; 29:4252–62. [PubMed: 19339619]

48. Banati RB, Rothe G, Valet G, Kreutzberg GW. Detection of lysosomal cysteine proteinases in microglia: flow cytometric measurement and histochemical localization of cathepsin B and L. Glia. 1993; 7:183–91. [PubMed: 8432559]

49. Yang CN, et al. Mechanism mediating oligomeric Aβ clearance by naïve primary microglia. Neurobiol Dis. 2011; 42:221–30. [PubMed: 21220023]

50. Cohen SIA, et al. Proliferation of amyloid-β42 aggregates occurs through a secondary nucleation mechanism. Proc Natl Acad Sci U S A. 2013; 110:9758–63. [PubMed: 23703910]

51. Koole M, et al. Whole-body biodistribution and radiation dosimetry of 18F-GE067: a radioligand for in vivo brain amyloid imaging. J Nucl Med. 2009; 50:818–22. [PubMed: 19372469]

52. Lin KJ, et al. Whole-body biodistribution and brain PET imaging with [18F]AV-45, a novel amyloid imaging agent--a pilot study. Nucl Med Biol. 2010; 37:497–508. [PubMed: 20447562]

53. Zhang X, et al. Design and synthesis of curcumin analogues for in vivo fluorescence imaging and inhibiting copper-induced cross-linking of amyloid beta species in Alzheimer's disease. J Am Chem Soc. 2013; 135:16397–409. [PubMed: 24116384]

54. Zhang X, et al. A bifunctional curcumin analogue for two-photon imaging and inhibiting crosslinking of amyloid beta in Alzheimer's disease. Chem Commun (Camb). 2014; 50:11550–3. [PubMed: 25134928]

55. Kayed R, et al. Permeabilization of lipid bilayers is a common conformation-dependent activity of soluble amyloid oligomers in protein misfolding diseases. J Biol Chem. 2004; 279:46363–6. [PubMed: 15385542]

56. Sepulveda FJ, Parodi J, Peoples RW, Opazo C, Aguayo LG. Synaptotoxicity of Alzheimer beta amyloid can be explained by its membrane perforating property. PLoS One. 2010; 5:e11820. [PubMed: 20676404]

57. Yoshiike Y, Chui DH, Akagi T, Tanaka N, Takashima A. Specific compositions of amyloid-beta peptides as the determinant of toxic beta-aggregation. J Biol Chem. 2003; 278:23648–55. [PubMed: 12716908]

58. Kuperstein I, et al. Neurotoxicity of Alzheimer's disease Aβ peptides is induced by small changes in the Aβ42 to Aβ40 ratio. EMBO J. 2010; 29:3408–20. [PubMed: 20818335]

59. Pauwels K, et al. Structural basis for increased toxicity of pathological aβ42:aβ40 ratios in Alzheimer disease. J Biol Chem. 2012; 287:5650–60. [PubMed: 22157754]

60. Jan A, et al. Abeta42 neurotoxicity is mediated by ongoing nucleated polymerization process rather than by discrete Abeta42 species. J Biol Chem. 2011; 286:8585–96. [PubMed: 21156804]

61. Streit WJ. Microglial senescence: does the brain's immune system have an expiration date? Trends Neurosci. 2006; 29:506–10. [PubMed: 16859761]

62. Cohen E, et al. Reduced IGF-1 signaling delays age-associated proteotoxicity in mice. Cell. 2009; 139:1157–69. [PubMed: 20005808]

63. Esparza TJ, et al. Amyloid-beta oligomerization in Alzheimer dementia versus high-pathology controls. Ann Neurol. 2013; 73:104–19. [PubMed: 23225543]

64. Grathwohl SA, et al. Formation and maintenance of Alzheimer's disease beta-amyloid plaques in the absence of microglia. Nat Neurosci. 2009; 12:1361–3. [PubMed: 19838177]
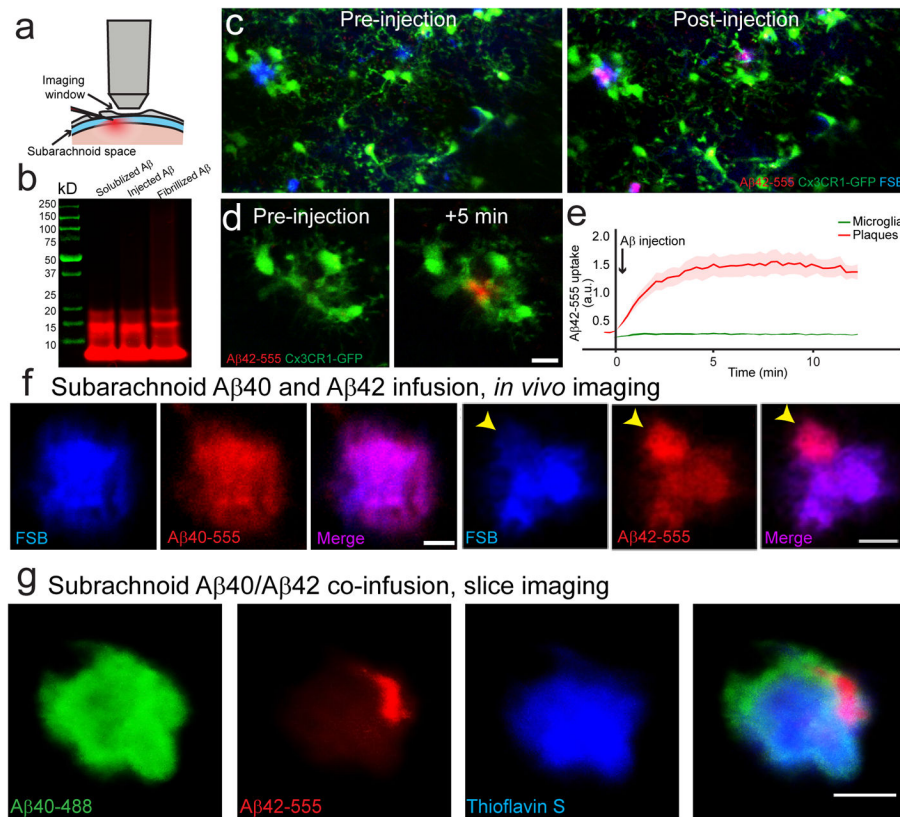
Figure 1. Microglia process envelopment of plaques is stable over weeks in vivo
(**a**) Representative confocal images of Iba1 immunolabeled microglia around Thioflavin S-labeled amyloid plaques in a 4-month-old 5xFAD mouse. (**b**) Quantification of microglia coverage in 4-month-old 5xFAD and 4-month-old CRND8 mice. Microglia coverage was quantified as the percentage of plaque perimeter contacted by microglia process. N>90 plaques (1–20 μm in diameter) from 5 animals for each transgenic line. Red bars represent mean ± s.e.m. (unpaired t test, $t_{(84)}2.998$ and $_{(156)}2.422$ in 5xFAD and $t_{(218)}2.379$ and $_{(362)}2.506$ in CRND8). (**c**) *In vivo* time-lapse images of microglia around amyloid plaques in *CX3CR1*-GFP x 5xFAD mouse. Blue arrows: microglia processes contacting amyloid plaques; red arrows: processes not in contact with amyloid plaque and extended between 20th and 30th minutes of the imaging session; red arrow-heads: processes not in contact with amyloid plaque and regressed between 20th and 30th minutes of the imaging session. (**d**) Quantification of microglia process stability over 30 minutes. N=15 plaques in 5 animals. Data represent mean s.e.m.. (**e** and **f**). *In vivo* time-lapse imaging over weeks to months reveals the stability of microglia processes contacting amyloid plaques. Stable processes: yellow arrows; newly added processes: red arrows; regressed processes: blue arrows. (**g**) Quantification of long-term dynamism of microglia processes contacting amyloid plaques. N=51 plaques in 9 animals. Scale bars: 5μm in **c**, **e** and **f**.

Figure 2. In vivo brain infusion reveals hotspots of Aβ42 binding to existing plaques
(**a**) Hylite-555 labeled Aβ40 or Aβ42 was infused into the mouse brain via the subarachnoid space and imaged through a thinned-skull window away from the injection site. (**b**) SDS-PAGE analysis of soluble Aβ42 used for in vivo infusion and ex vivo brain slice labeling. Fluorescently-labeled Aβ42 stock solution (DMSO, 1μg/μl) was diluted in ACSF (1:9 v/v) on ice. Three different preparations of Aβ42 were analyzed using SDS-PAGE gel. The SDS-PAGE analysis indicated that the main Aβ species injected were monomers and small oligomers. (**c** and **d**) *In vivo* two-photon time-lapse images in *CX3CR1*/5XFAD mice show that Aβ42-555 (red) rapidly binds to existing amyloid plaques, pre-labeled by FSB (blue) that are extensively surrounded by microglia (green). (**e**) Quantification of Aβ42-555 fluorescence during injection. Aβ42-555 binds to pre-existing amyloid plaque rapidly and with very high specificity. Internalization by surrounding microglia was undetectable in this time-frame. N=30 plaques in 5 animals. Data represents mean ± s.e.m.. (**f**) High magnification two-photon images show hotspots of Aβ42-555 binding to amyloid plaques (arrowhead). In contrast Aβ40-555 infusions led to homogeneous binding to amyloid plaques. (**g**) Simultaneous *in vivo* infusion of Aβ42-555 and Aβ40-488 followed by confocal imaging in fixed slices.
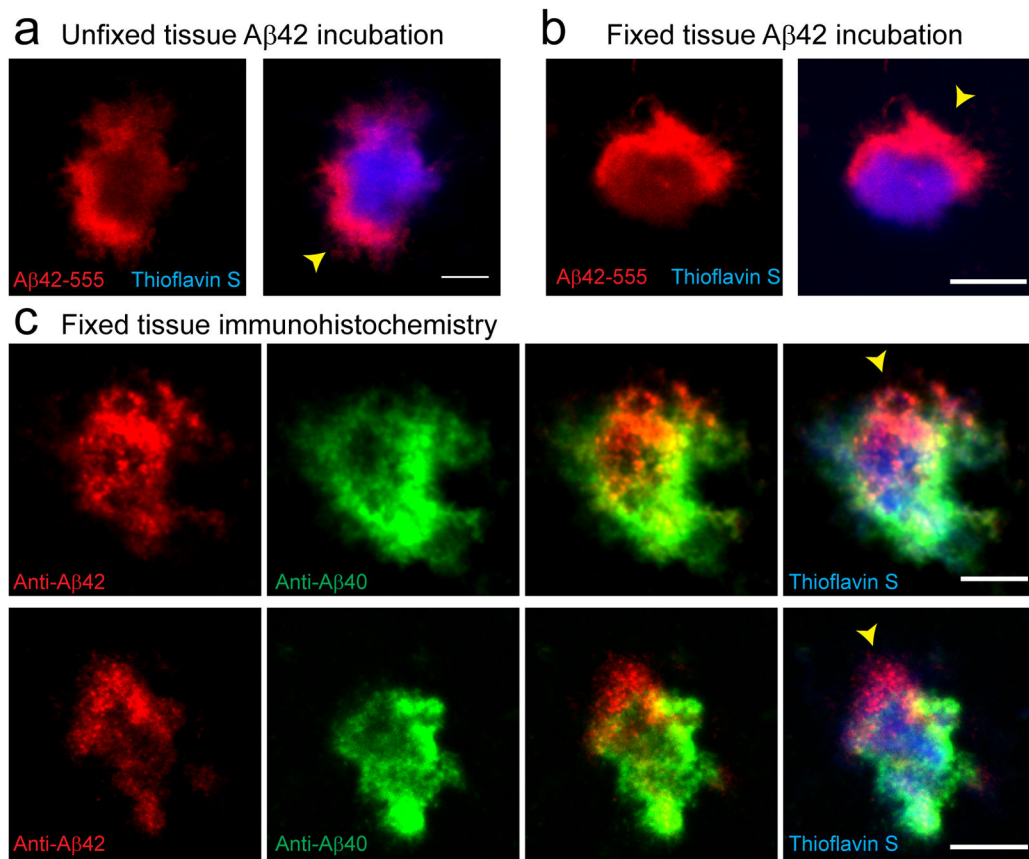
Figure 3. Endogenous Aβ42 accumulates within plaque hotspots in vivo
(**a** and **b**) Representative confocal images show hotspots of Aβ42-555 binding (arrowheads) in fresh unfixed (**a**) and fixed-permeabilized brain slices (**b**). (**c**) Immunohistochemistry with Aβ42 and Aβ40 c-terminus specific antibodies on fixed brain slices from mice that did not receive an Aβ-555 injections. Scale bars: 5μm in all panels.
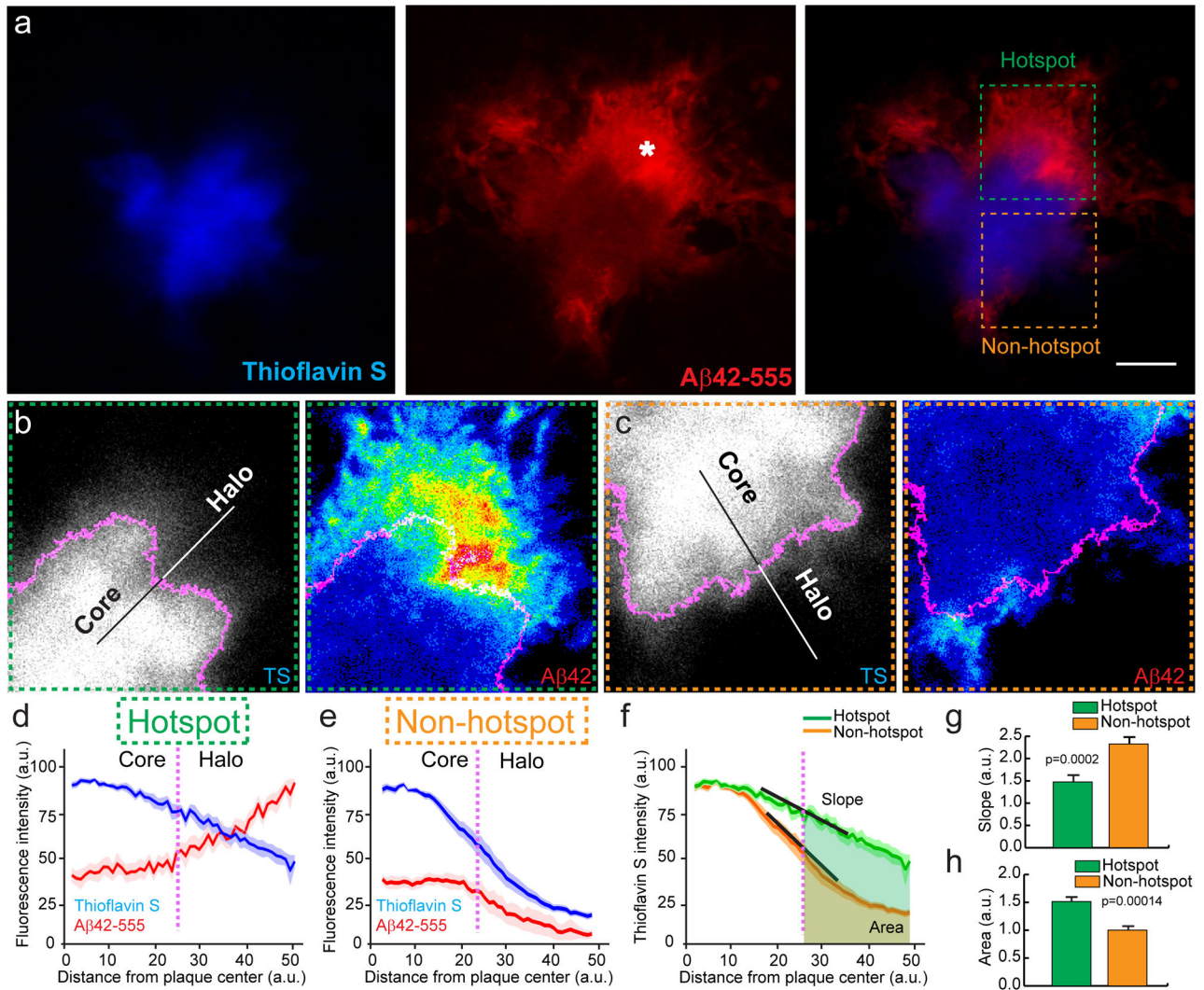
Figure 4. Aβ42 hotspots occur in distinct plaque regions with sparse fibrillar amyloid
(**a**) Representative confocal images of Aβ42-555 binding to fibrillar amyloid plaque
(asterisk indicates a prominent Aβ42 hot-spot). Scale bar: 5μm. Dashed squares point to
areas with (green) and without (orange) an Aβ42 hotspot. (**b, c**) Intensity (heat) maps of
plaque borders pointing towards a hotspot (**b**) and a non-hotspot (**c**) area, depicted at low
zoom in (**a**). The magenta outline in **b** and **c** represents the thresholded plaque border
separating the plaque core from the halo. (**d,e**) Line profiles of fluorescence intensities
across the plaque borders (magenta dotted lines) as shown in **b** and **c**. Data represents mean
± s.e.m. (**f–h**) Quantification of thioflavin S fluorescence change as a function of distance
from the plaque center in hotspot and non-hotspot areas. The slope of the curves indicates
the rate of fluorescence change (how compact are the fibrils at the plaque edge) and the area
under the curve represents the amount of fibrillar amyloid (total TS fluorescence) in the
plaque halo area. Data represents mean ± s.e.m. (unpaired t-test, $t_{(47)}$4.005 in (**g**),
$t_{(34)}$4.299 in (**h**)). For (**d–h**) N=30 plaques with diameter less than 10μm from 2 5xFAD
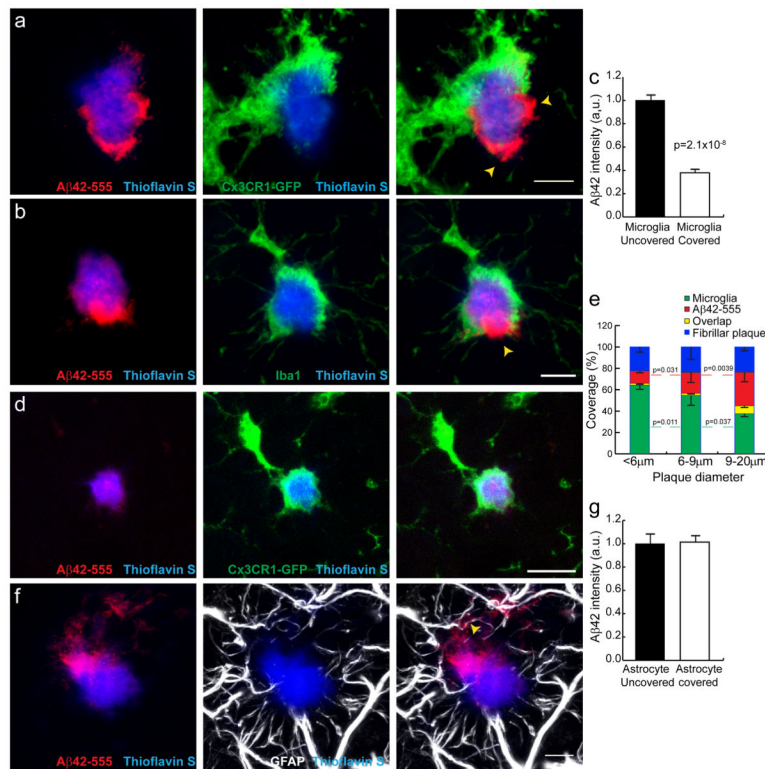mice (6-month-old).

Figure 5. Microglia but not astrocyte processes are anti-colocalized with Aβ42 hotspots
(**a,b**) Representative Confocal images of Aβ42 hotspot (arrowheads) and surrounding microglia. Microglia were labeled by cross breeding with *CX3CR1*-GFP mice. (**b**) Quantification of Aβ42-555 fluorescence in areas covered or uncovered by microglia. N=60 plaques from 3 mice. Data represents mean ± s.e.m. (unpaired t-test, t=$_{(58)}$6.309). (**c–e**) Microglia coverage decreases as plaques grow while Aβ42 hotspot becomes more prominent. Small plaques tend to be completely wrapped by microglia without hotspot (**d**). Quantification of plaque perimeters in different size groups show that plaque size negatively correlated with microglia coverage, while positively correlated with Aβ42 hotspot (**e**). N=60 plaques from 3 mice. Data represents mean ± s.e.m; corresponding groups in each plaque size bin were compared with unpaired t-test (t=$_{(30)}$2.728 and $_{(22)}$2.218 for microglia coverage. t=$_{(30)}$2.253 and $_{(22)}$3.223 for Aβ42 coverage). (**f,g**) Astrocytic processes (labeled with GFAP) around amyloid plaques do not correlate with Aβ42 hotspot. N=60 plaques from 3 mice. Data represents mean ± s.e.m.. Scale bars: 5μm in all panels.
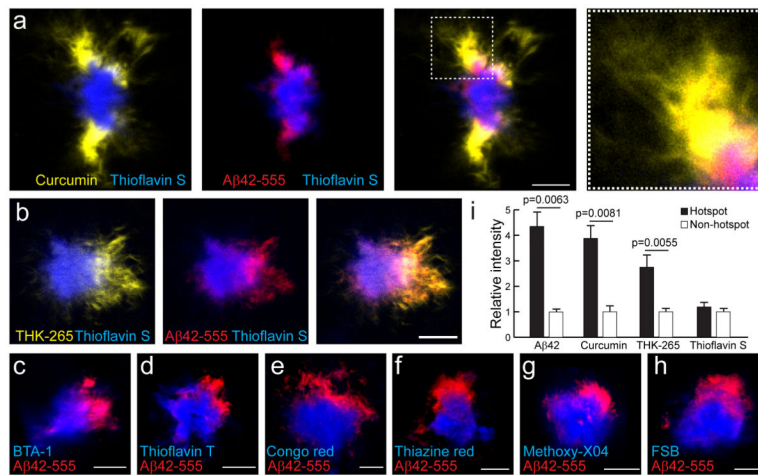
Figure 6. Unique plaque-labeling patterns of Aβ binding dyes

(**a–h**) Representative confocal images in fixed slices demonstrate unique labeling patterns for various β-sheet binding dyes. In vivo subarachnoid infusion of Aβ42-555 (red) was performed 1 day before slice dye labeling. Scale bars: 5μm. (**i**) Quantification of different β-sheet binding dyes labeling in Aβ42-555 hotspot and non-hotspot areas. N>10 plaques for each dye. Data represents mean ± s.e.m. (unpaired t-test, $t=_{(14)}3.210$, $_{(14)}3.090$ and $_{(15)}2.900$).
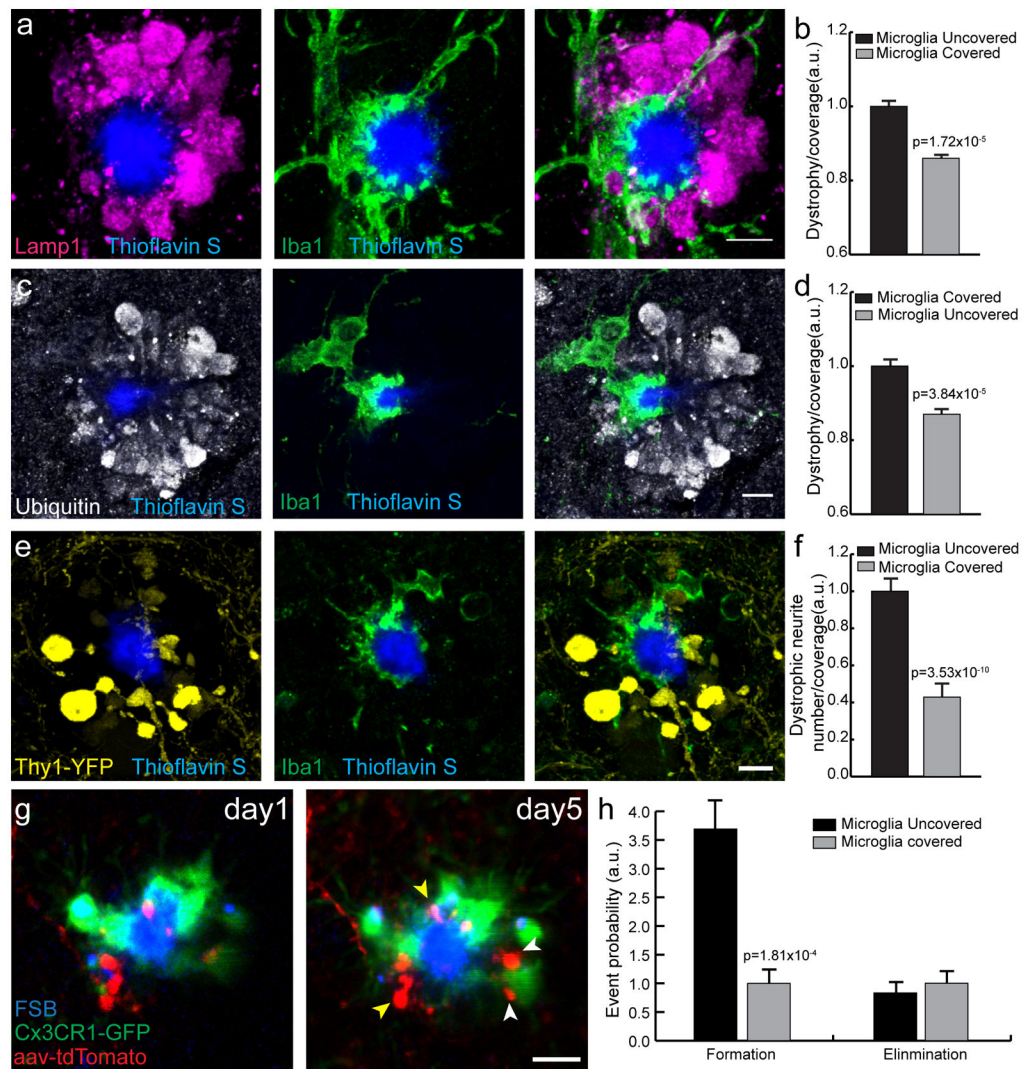
Figure 7. Microglia processes protect adjacent neurites from protofibrillar Aβ42 toxicity
(**a–d**) Representative confocal image analysis of the degree of microglia coverage (Iba1, green) versus extent of neuritic dystrophy (Lamp1, magenta or Ubiquitin, grey). Graphs in **b, d** represent the area of dystrophic neurites extending radially outward from microglia covered or uncovered plaque perimeter. The degree of neuritic dystrophy (Y axis) is normalized by the angular plaque coverage by microglia processes (see methods for detail). N>60 plaques from 3 mice. Data represents mean ± s.e.m. (paired t-test, $t_{(57)}$4.694 in (**a**) and $_{(67)}$4.410 for (**b**)). (**e,f**) Representative confocal images of microglia and dystrophic neurites around amyloid plaques in Thy1-YFP/5xFAD mice. Quantification of dystrophic neurite number was done as in **b and d**. N=70 plaques from 4 mice. Data represents mean ± s.e.m. (paired t-test, $t_{(67)}$8.290). (**g,h**) Two-photon transcranial *in vivo* time-lapse images of dystrophic neurite dynamics around amyloid plaques. Newly formed (white arrowhead) and stable (yellow arrowhead) dystrophic neurites (labeled in either Thy1-YFP mice or by AAV-TdTomato injections) were quantified (data is a combination of both labeling methods).

Data comes from 8 mice and 45 plaques. Data represents mean ± s.e.m. (paired t-test, $t=_{(42)}4.108$). Scale bars represent 5μm in all panels.
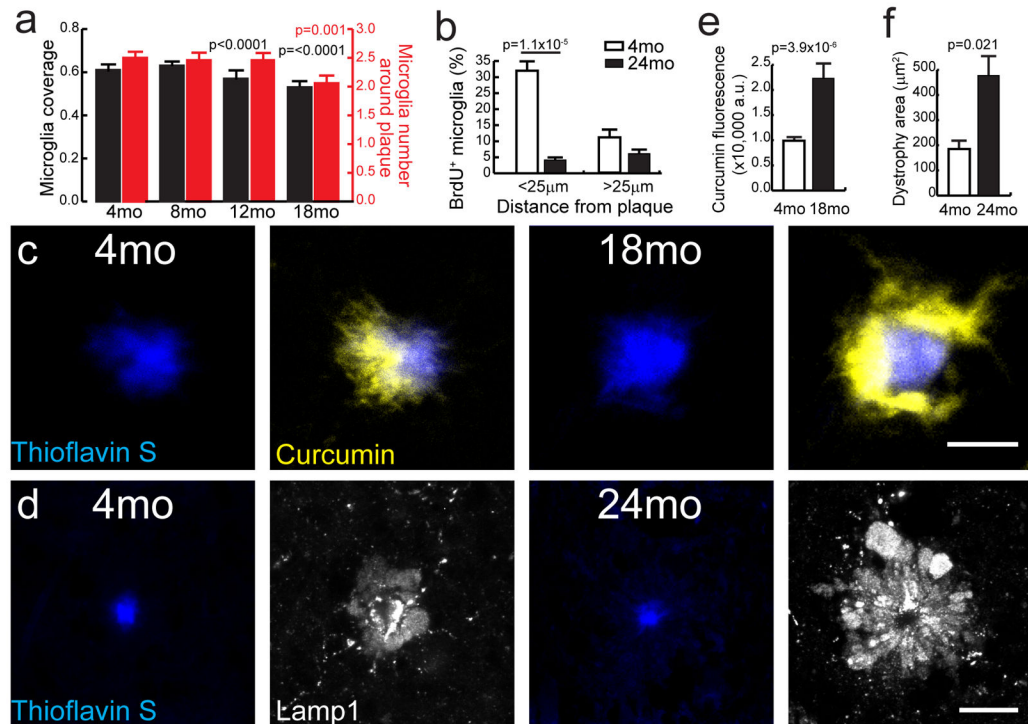
Figure 8. Reduced microglia coverage in aging is associated with an increased Aβ halo and neurotoxicity

(**a**) Quantification of microglia coverage (black bars) and microglia number (red bars) within 25μm from the plaque edge at different ages in CRND8 mice. N>120 plaques from 4 mice per age group. Data represents mean ± s.e.m. (unpaired t-test, $t=_{(373)}3.905$ and $_{(286)}5.602$ in microglia coverage and $t=_{(286)}3.325$ in microglia number). (**b**) Quantification of BrdU+ microglia in 4mo and 24mo CRND8 mice. N=222 and 100 field of views analyzed for 24 and 4 month-old mice, respectively. Data represents mean ± s.e.m. (unpaired t-test, $t=_{(159)}4.374$). (**c, d**) Representative confocal images of Aβ halo (labeled with curcumin in **c**) and neuritic dystrophy (labeled with Lamp1 immunohistochemistry in **d**) in CRND8 mice. Scale bars represent 5μm in all panels. (**e, f**) Quantification of curcumin labeled protofibrillar Aβ halo (**e**) and Lamp1-labeled neuritic dystrophy area (**f**). N=62 plaques in (**e**) and 44 plaques in (**f**). Data represents mean ± s.e.m. (unpaired t-test, $t=_{(60)}5.508$ for (**e**) and $_{(40)}2.404$ for (**f**)).
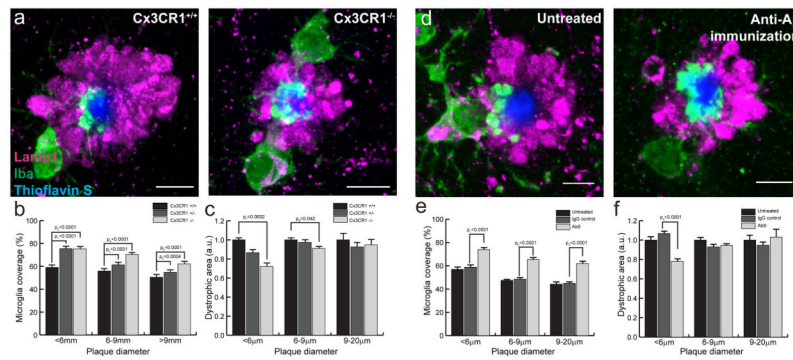
Figure 9. *CX3CR1* deletion or Aβ immunization increases microglia coverage and reduces dystrophy

(**a**) Representative confocal images of microglia coverage and dystrophic neurites in 8mo CRND8 mice harboring different copy numbers of *CX3CR1* gene. (**b**) Quantification of microglia coverage as a function of *CX3CR1* genotype and plaque size. $t_1=_{(140)}7.465$, $t_2=_{(159)}8.939$, $t_3=_{(202)}5.890$, $t_4=_{(249)}13.28$, $t_5=_{(56)}3.760$, $t_6=_{(47)}5.784$. (**c**) Quantification of dystrophic neurite area as a function of *CX3CR1* genotype and plaque size. $t_7=_{(170)}3.828$, $t_8=_{(256)}2.047$. (**d**) Representative confocal images of microglia coverage and dystrophic neurites in 4mo 5xFAD mice treated with passive anti Aβ immunization for 8 weeks. (**e**) Quantification of microglia coverage as a function of treatment and plaque size. $t_1=_{(324)}8.093$, $t_2=_{(385)}15.59$, $t_3=_{(66)}5.848$. (**f**) Quantification of dystrophic neurite area as a function of treatment and plaque size. $t_4=_{(218)}4.557$. For all quantifications data represents mean ± s.e.m and compared using unpaired t-tests. In each genotype or treatment N>3 animals and 40 plaques per animal. Scale bars: 5μm in all panels.